Thermal generation, manipulation and detection of skyrmions

Zidong Wang[1,2,*], Minghua Guo[1,3,*], Heng-An Zhou[1,2,*], Le Zhao[1,2*], Teng Xu[1,2], Riccardo Tomasello[4], Hao Bai[1,2], Yiqing Dong[1,2], Soong Geun Je[5,6], Weilun Chao[5], Hee-Sung Han[7], Suseok Lee[7], Ki-Suk Lee[7,8], Yunyan Yao[9], Wei Han[9], Cheng Song[10], Huaqiang Wu[3], Mario Carpentieri[11], Giovanni Finocchio[12], Mi-Young Im[5,8], Shi-Zeng Lin[13,†] and Wanjun Jiang[1,2,†]

[1]*State Key Laboratory of Low-Dimensional Quantum Physics and Department of Physics, Tsinghua University, Beijing 100084, China*

[2]*Frontier Science Center for Quantum Information, Tsinghua University, Beijing 100084, China*

[3]*Institute of Microelectronics, Tsinghua University, Beijing 100084, China*

[4]*Institute of Applied and Computational Mathematics, FORTH, GR-70013, Heraklion-Crete, Greece*

[5]*Center for X-ray Optics, Advanced Light Source, Lawrence Berkeley National Laboratory, Cyclotron Road, Berkeley, CA 94720, USA*

[6]*Department of Physics, Chonnam National University, Gwangju 61186, Korea*

[7]*School of Materials Science and Engineering, Ulsan National Institute of Science and Technology, Ulsan 44919, Korea*

[8]*Daegu Gyeongbuk Institute of Science and Technology, Daegu 711-873, Korea*

[9]*International Center for Quantum Materials, School of Physics, Peking University, Beijing, 100871, China*

[10]*Key Laboratory of Advanced Materials (MOE), School of Materials Science and Engineering, Tsinghua University, Beijing 100084, China*

[11]*Department of Electrical and Information Engineering, Polytechnic of Bari, Bari 70125, Italy*

[12]*Department of Mathematical and Computer Sciences, Physical Sciences and Earth Sciences, University of Messina, Messina 98166, Italy*

[13]*Theoretical Division, T-4 and CNLS, Los Alamos National Laboratory, Los Alamos, New Mexico 87545, USA*

[*] These authors contributed equally to this work.

[†] To whom correspondence should be addressed:

jiang_lab@tsinghua.edu.cn, szl@lanl.gov.

Recent years have witnessed significant progresses in realizing skyrmions in chiral magnets[1-4] and asymmetric magnetic multilayers[5-13], as well as their electrical controls[2,7,8,10]. Equally important, thermal control of skyrmions including thermal generation, manipulation and detection of skyrmions can be exploited for prototypical new architecture with integrated computation[14] and energy harvesting[15]. It has yet to verify if skyrmions can be purely generated by heating[16,17], and if their resultant direction of motion driven by temperature gradients follows the diffusion or, oppositely, the magnonic spin torque[17-21]. Here, we address these important issues for the first time? in microstructured devices made of asymmetric multilayers – $[Ta/CoFeB/MgO]_{15}$, $[Pt/CoFeB/MgO/Ta]_{15}$ and $[Pt/Co/Ta]_{15}$ integrated with on-chip heaters, by using a full-field soft X-ray microscopy. The thermal generation of densely packed skyrmions is attributed to the low energy barrier at the device edge, together with the thermally induced morphological transition from stripe domains to skyrmions. The unidirectional diffusion of skyrmions from the hot region towards the cold region is experimentally observed. It can be theoretically explained by the combined contributions from repulsive forces between skyrmions, entropic forces[17,18,20-22] and thermal spin-orbit torques in competing with the magnonic spin torques. These thermally generated skyrmions can be further electrically detected by measuring the accompanied anomalous Nernst voltages[23]. The on-chip thermoelectric generation, manipulation and detection of skyrmions could open another exciting avenue for enabling skyrmionics, and promote the interdisciplinary study between the spin caloritronics[15], magnonics[24] and skyrmionics[3,4,12].

The nontrivial spin topology and particle-like behaviors of skyrmions have recently stimulated immense interests in the spintronics community[4,12,25]. For practical applications, efficient generation, manipulation and detection of skyrmions are essential. In this regard, electrical currents and/or current-induced spin-orbit torques (SOTs) are conveniently utilized in various metallic systems[2,8,10]. However, a pure thermal generation, manipulation and detection of skyrmions have not been studied experimentally, which motivate the present study. Such experiments, while remaining challenge in bulk samples and large-area films, can be done in microstructured devices integrated with on-chip heaters. Namely, elevating local

temperatures facilitates the skyrmion formation out of other competing magnetic phases by overcoming the corresponding energy barriers[16,17]. A successful demonstration of the proposed experiments could provide a new approach that can be particularly useful for studying skyrmions and their dynamics in magnetic insulators[26,27], and may lead to various technologically relevant physics/device concepts to be investigated[14].

Experimental demonstration of thermal generation of skyrmions.

The interfacially asymmetric multilayers used in the present study are: $[Ta/Co_{20}Fe_{60}B_{20}/MgO]_{15}$, $[Pt/Co_{60}Fe_{20}B_{20}/MgO/Ta]_{15}$ and $[Pt/Co/Ta]_{15}$, which were typified with a monotonic increase of the interfacial Dzyaloshinskii-Moriya interaction (DMI) strengths[8,10,13,28] and damping paramters[10]. Magnetometry measurements reveal typical hysteresis loops that are reminiscence of multilayers hosting Néel-type skyrmions[10,11,13]. Since the size of skyrmions in multilayers are generally smaller than 200 nm, we employed a soft X-ray full-field transmission microscope (XM-1) with a spatial resolution down to 20 nm at the beamline 6.1.2 at the Advanced Light Souce of Lawrence Berkeley National Laboratory[10]. Rich sample environment of XM-1 enables the dynamics of skyrmions stimulated by perpendicular magnetic field ($\mu_0 H_\perp$), electrical current (j_e), temperature (T) and temperature gradient ($\Delta T(x)$) to be investigated. Magnetic imagings were conducted at the Fe L_3 edge (708.5 eV) in the $[Ta/Co_{20}Fe_{60}B_{20}/MgO]_{15}$, and at the Co L_3 edge (778.5 eV) in the $[Pt/Co_{60}Fe_{20}B_{20}/MgO/Ta]_{15}$ and the $[Pt/Co/Ta]_{15}$ multilayers. We focus on the $[Ta/Co_{20}Fe_{60}B_{20}/MgO]_{15}$ multilayers for which exhibit the strongest X-ray magnetic circular dichroism (XMCD) contrast, unless otherwise specified. The evolution of domain configurations as a function of $\mu_0 H_\perp$ is shown in the Supplementary Materials. The coexisting stripe domains and sparsely distributed skyrmions at low field (< 10 mT) suggest densely packed skyrmion lattice is not the ground state. Note that the dominant features of the thermal generation of skyrmions in these three multilayers remain the same, indicating the phenomenology revealed in our experiments are generic in skyrmion hosting multilayers.

We have designed and fabricated devices by integrating magnetic multilayers with on-chip heaters and thermometers made of Ta (20 nm)/Pt (50 nm) for *in-situ* control/measure of temperatures and anomalous Nernst measurements. Those devices were prepared onto the insulating Si_3N_4 (100 nm thick) membranes, in order to ensure X-ray transmission imaging.

Optical image of the device is shown in Fig. 1A. By applying a pulse voltage (V_h) into the Ta/Pt heater, a local temperature gradient is created through heat dissipation in the underneath insulating Si_3N_4 thin layer. The dissipated heat arrives at the multilayer that could generate skyrmions from different background orderings. Furthermore, the accompanied temperature gradient $\Delta T(x)$ produces diffusion of skyrmions, and allows an electrical detection of thermally generated skyrmions via measuring the anomalous Nernst voltage (V_{ANE}) between two contacts ($C_{1,2}$). Additionally, symmetric heaters located on both sides of multilayer enable the directional control of skyrmion generation. Calibrations of temperatures and temperature gradients were discussed in the Supplementary Materials, which suggest the existence of quasilinear temperature gradients in the multilayer. For the maximum voltage applied into the Ta/Pt heater, the Oersted fields at the multilayer were calculated to be less than 0.22 mT, thus their influence on skyrmion dynamics is negligible. The threshold depinning electrical current (below which skyrmions do not move), is estimated to be larger than $J_{th} \geq 1\times10^5 A/cm^2$ by applying electrical currents to the multilayers[13].

The temperature profile across the whole device on the 100 nm-thick Si_3N_4 membrane ($500\times500\,\mu m^2$) was computed by the COMSOL Multiphysics software with the material specific parameters, as shown in Fig. 1B. Detailed descriptions are given in the Method section and in the Supplmentary Materials. A linescan of the device (cyan line) is shown in the lower panel of Fig. 1B, which confirms the spatially varying temperature profile along the *x*-axis. For different voltages V_h applied to the upper heater (H1), temperatures of both heaters ($T^S_{H1,2}$) and the upper/lower edges of the multilayer channel ($T^S_{U,L-E}$) in the imaging area were simulated and shown in the left panel of Fig. 1B. From the temperature difference between T^S_{U-E} and T^S_{L-E} of the multilayer, a linear temperature gradient $\Delta T(x)$ along the x-axis in the multilayer is estabilished. The experimentally measured temperatures of both heaters (H1,2) agree with the COMSOL simulations.

Representative images of thermal generation of skyrmions in the $[Ta/Co_{20}Fe_{60}B_{20}/MgO]_{15}$ multilayers under positive (negative) magnetic fields are shown in Fig. 1C (1D). When a pulse voltage of duration 100 μs and amplitude V_h=¿0.59 V is applied across the upper heater (H1), the original disordered stripe domains immediately transform into densely packed skyrmions, as shown in Fig. 1C for $\mu_0 H_\perp$ = -25.6 mT and Fig. 1D for

$\mu_0 H_\perp$ = +25.4 mT, respectively. Since skyrmion topological charge $Q=\frac{1}{4\pi}\int m\cdot(\partial_x m\times\partial_y m)\,dxdy$ is an odd function of the normalized magnetization m, it switches its sign under reversed external magnetic fields, as evidenced by the opposite color contrasts in Figs. 1C and 1D. The temperature at the upper edge is $T^S_{U-E}=399.3\,K$, and calculated average temperature gradient in the multilayer is $\Delta T(x)=1.6\,K/\mu m$, respectively. The diameter of skyrmion is estimated to be around 140 nm by fitting the skyrmion profile, and the skyrmion density is 6.8/μm^2. Note that similar phenomena shown in Fig. 1C(1D) can also be repeated by using the lower heater (H2) located on the opposite sides of multilayer, as shown in the Extended Data S4.

To resolve the detailed intermediate processes of the skyrmion generation, a sequence of smaller pulse voltages were adopted to reduce the generation efficiency. At $\mu_0 H_\perp$= -19.3 mT, stripe domains prevail in the multilayer. Following the increased number of pulses, three distinct behaviors are identified, as shown in Fig. 2A: (1) Nucleation of skyrmions from the hot edge. (2) Transformation from the existing stripe domains into isolated skyrmions. (3) The unidirectional motion of thermally generated skyrmions from the hot region towards the cold region. Intriguingly, under a saturated ferromagnetic (FM) background, coexisting stripe domains and isolated skyrmions can also be generated near the hot edge and from the interior of multilayers (presumably around structural defects for which exhibits a low topological energy barrier[29]), as shown in Fig. 2B. These characteristics can be clearly seen in the Extended Data S1-S3 and in the Supplementary Movies.

Fig. 2C illustrates the thermal generation of skyrmions in the $[Pt/Co/Ta]_{15}$ multilayer from a fully saturated FM background ($\mu_0 H_\perp$ = -47.8 mT). The sizes of skyrmions are around 95 nm in this multilayer, owing to the elevated DMI strength. After applying a pulse voltage (100 μs and V_h=¿0.68 V, $T^S_{U-E}=436\,K$) across the upper heater (H1), skyrmions are solely generated from the hot edge, and then propagate towards the cold edge upon applying the next pulse voltage. Note that the pinning effect of skyrmions in the $[Pt/Co/Ta]_{15}$ is strong, compared with $[Ta/Co_{20}Fe_{60}B_{20}/MgO]_{15}$ and $[Pt/Co_{60}Fe_{20}B_{20}/MgO/Ta]_{15}$ multilayers[10]. The representative thermal generation of skyrmions in the $[Pt/Co_{60}Fe_{20}B_{20}/MgO/Ta]_{15}$ is also provided in Extended Data S5. Since both the pinning effect and the magnetic damping

intimately correlate with the structural inhomogenieties or defects, we empirically used the damping parameter (α) as an indicator to show the effect of pinning on skyrmion generation. As shown in Fig. 2D, a monotonic increase of threshold temperatures (T_{U-E}^{th}) are required to produce densely packed skyrmion phase ($\mu_0 H_\perp$ = +24.6 mT). Since a large damping parameter reduces the thermal activation rate of skyrmion crossing the energy barrier, it raises T_{U-E}^{th}. Other factors such as exchange interactions, boundary geometry are also important in determining T_{U-E}^{th}, which requires further investigations.

To quantify the skyrmion generation rate as a function of pulse duration and amplitude, skyrmions in images of Figs. 2A-2B were counted. When $T_{U-E}^{S} > 375\,K$ (intercept at the *x* axis), the increased T_{U-E}^{S} results in a linear increase of skyrmion generation rate by 9/ K, as shown in Fig. 2E. The linear behavior is due to the small temperature window about 10 K compared to the based temperature. The intercept at 375 K marks a threshold temperature where substantial skyrmions are generated after applying pulse voltage with duration 100 μs. The energy barrier for skyrmions nucleation is expected to be greater than 375 K because the pulse duration is much longer than the microscopic time scale. A phase diagram summarizing the evolution of stripe domains, coexisting stripe domains and skyrmions, densely packed skyrmion lattice and saturated FM states as a function of magnetic field and temperature of the hot edge (T_{U-E}^{S}) is summarized in Fig. 2F for the $[Ta/Co_{20}Fe_{60}B_{20}/MgO]_{15}$ multilayer. A similar phase diagram on the duration of pulse voltages (V_h=¿ 0.53 V) and $\mu_0 H_\perp$ is also displayed in the Extended Data S6. In both phase diagrams, four different magnetic phases can be clearly distinguished. When magnetic fields are small ($|\mu_0 H_\perp| < 10\,mT$), increase of T_{U-E}^{S} only result in a configurational change of stripe domains. This is due to the fact that skyrmion phase is locally unstable under a weak magnetic fields. When $|\mu_0 H_\perp| > 10\,mT$, thermal fluctuation in the range of $375\,K < T_{U-E}^{S} < 397\,K$ produces a coexisting phase of stripe domains and sparesely distributed skyrmions. This can be attributed to the stochastic nature of the thermally assisted skyrmion nucleation by overcoming the energy barrier separating the skyrmion and the stripe phase. At higher $T_{U-E}^{S} > 397\,K$, thermal fluctuations further promote the nucleation of skyrmions and the system enters densely packed skyrmion lattice. At higher $|\mu_0 H_\perp| > 45\,mT$, the system remains in the FM state in the experimentally accessible temperature range, which indicates that the FM state is the globally stable state in this field region[30].

Diffusion of skyrmions driven by temperature gradients

When skyrmion generation is efficient at the hot edge, there exists an increased repulsive force between the newly generated skyrmions and the existing skyrmions. This naturally results in a directional diffusive motion of skyrmions from the hot region towards the cold region. However, this directional diffusion can be also attributed to the temperature gradient in the sample, where skyrmions move towards the cold edge driven by the entropic force due to the entropy gradient. To separate these two mechanisms, we designed a nanowire pointing to the heater. Skyrmion generation at the hot end is minimized due to the tip-like geometry, as shown in Fig. 3A. In fact, the implementation of this type of device may enable a single skyrmion to be generated in a controllable manner. Additionally, the skyrmion generation can also be suppressed if one controls the temperature at the tip (T^{S}_{U-E}) to be lower than the threshold temperature for skyrmion generation (T^{th}_{U-E}), as guided by the phase diagram shown in Fig. 2F. After applying pulse voltages of duration 500 ms and amplitudes in the range of 0.18 - 0.23 V (corresponding to $338K < T^{S}_{U-E} < 365K$) into the heater, the thermal generation of skyrmion is completely suppressed. The resulting directional diffusion driven by temperature gradients along the nanowire is clearly observed, with $\Delta T(x)$in the range of $0.29K/\mu m - 0.56K/\mu m$, as shown in Figs. 3A. Note that a few skyrmions were annihilated upon applying a larger $\Delta T(x)$. During the diffusion, sparsely distributed skyrmions were aligned in the centre of the $[Ta/Co_{20}Fe_{60}B_{20}/MgO]_{15}$ nanowire, which can be clearly seen from the stochastic trajectory shown in Fig. 3A-8. This occurs as a result of the balanced skyrmion-edge interaction from both edges[31]. Note here skyrmions move from hot region to the cold region, in line with the directional Brownian motion. In skyrmion materials, theory predicted another magnonic spin torque mechanism, under which, skyrmions move from cold to hot instead [15, 18]. Our experiment clearly indicates that the magnon transport is greatly suppressed and the Brownian-like diffusion prevails. By taking the ratio between displacements and pulse durations, the diffusion velocity is also calculated and shown in Fig. 3A-9. The observed nonlinear velocity and the absence of skyrmion Hall effect is consistent with the stochastic nature of diffusion. Nevertheless, our experiments clearly show that the thermal diffusion of skyrmions is dominant over the opposite motion driven by magnonic spin torque[17,18,20].

Theory on the skyrmion generation and dynamics

All of the aforementioned experimental observations can been well addressed in a unified theoretical setting as follows. In our multilayer, there exist competing metastable phases: stripe domains, mixture of stripe domains and skyrmions, skyrmion lattices and saturated FM states. Near the (hot) edge, skyrmions can be generated without meeting any sigularity. Together with the twisted edge spins by the unbalanced interfacial DMI[29,32], the topological energy barriers for skyrmion generation is relatively low. Local heating at the edge could thus effeciently facilitate skyrmion generation from different magnetic phases. Our calculations based on the statistical rate theory[33] and Monte Carlo simulations given in the Supplementary Materials confirm that the edge is the dominant source for skyrmion generation. Note that skyrmions can also be generated from the structural defects in the interior of multilayers, and by coalescing of the stripe domains[34], which also exhibit low energy barriers.

Our experiments can be numerically reproduced by solving the stochastic Landau-Lifshitz-Gilbert equation in the presence of temperature gradients. In our micromagnetic simulation, other sources that could influence the dynamics of skyrmions, including the thermal spin Hall effect, the magnonic spin torques arising from thermally excited magnons[17,18,20], and the repulsive interaction between skyrmions are taken into account self-consistently. The system Hamiltonian reads as $H=\frac{J_{ex}}{2}(\nabla \mathrm{S})^{2}+D\left[S_{z}(\nabla\cdot S)-(S\cdot\nabla)S_{z}\right]-H_{a}\cdot S$ with J_{ex} being the strength of exchange interaction, $D$the interfacial DMI parameter, and H_a the perpendicular magnetic fields. The equation of motion for spins (S) can be written as:

$$\partial_t S=-\gamma S\times(H_{eff}+h_n)+\alpha S\times\partial_t S, \qquad (1)$$

where γ is the gyromagnetic ratio, $H_{eff}=-\delta H/\delta S$ is the effective field, h_n is the random thermal fluctuating field at$T(x)=kx$, and α is the damping parameter. The choice of k is to ensure the temperature at the hot edge (T^{S}_{U-E}) is comparable to the energy barrier Δ, such that appreciable numbers of skyrmions can be generated at the hot region in the time scale of simulations. Using the saturated FM state as an initial state, the thermal generation of skyrmions from the hot edge of devices that is followed by a unidirectional diffusion towards the cold region is evident, as shown in Fig. 3B. If periodic stripe domains were used as the initial state instead, similar results were obtained in the simulation. In particular, skyrmion

generation from the hot edge, their subsequent directional diffusion towards the cold region, together with a morphological transition from stripe domains to isolated skyrmions, were identified and shown in the Extended Data S7. In both cases, the multilayer is eventually filled with densely packed skyrmions. Once the temperature at the hot side is reduced, skyrmion nucleation is suppressed, and our simulation reproduces thermal diffusion of skyrmions driven by a temperature gradient reported in Fig. 3, as shown in the Extended Data S8. Using materials specific parameters, a layer resolved micromagnetic simulation is also conducted in which the thermal geneneration and diffusion can be reproduced in the Part 14 of the Supplementary Materials..

Assuming skyrmion diffusion is much faster than the skyrmion generation rate, the skyrmion-skyrmion repulsive interaction can be neglected. In this case, the thermal diffusion of a skyrmion driven by temperature gradients can be studied (as experimentally demonstrated in Fig. 3A). After establishing the local thermal equilibrium with a linear $\Delta T(x)$, the thermal generation and subsequent diffusion of skyrmions can be described by the Fokker-Planck equation in dimensionless units as follows[17,20]:

$$\partial_t \acute{P} + \partial_x \left[\acute{F}_m \acute{P} \right] - G_{xx} \partial_x (T \partial_x \acute{P}) = \omega_s \exp\left[\frac{-\Delta}{k_B T} \right], \qquad (2)$$

where $\acute{P}(x)$ is the probability of finding skyrmions at time t and at the position x. The second term on the left describes the average drift velocity $(\acute{F}_m)$ of skyrmion due to the magnonic spin torque and the spin torque generated by thermoelectric currents, in competition with pinning force due to defects. The third term on the left describes the diffusion of skyrmions with G_{xx} being the gyrotropic coupling component. The term at the right side of Eq. (2) corresponds to the thermal activation of skyrmions with Δ being the energy barrier and ω_s being the attempt frequency. In the regime $k_B T \ll \Delta$, skyrmion nucleation is greatly suppressed. Under small temperature gradient, $\acute{F}_m \acute{P} \gg G_{xx} T \partial_x \acute{P}$. When the pinning is weak, free drift of the existing skyrmions can be enabled, and the direction of motion depends on the relative strength of the magnonic spin torque and SOT of thermoelectric currents. However, in the presence of temperature gradients in our multilayers, the thermal spin Hall effect, thermal magnon currents were estimated to be smaller than the threshold depinning current density $J_{th} \geq 1 \times 10^5 A/cm^2$, so neither of them can produce skyrmion motion. In this strong pinning limit, thermal diffusion of the skyrmion thus dominates.

When $k_B T$ is comparable with Δ, the thermally assisted skyrmion generation becomes important. Subsequently, the dynamics is governed by the diffusion of skyrmions from the hot region towards the cold region. For a clear demonstration, the time evolution of the skyrmion densities for varying amplitudes of $\acute{F}_m = 0.2$ and $\acute{F}_m = 0$ are calculated and shown in Figs. 3C and 3D, respectively. It is evident that skyrmions can be thermally nucleated at the hot edge regardless the choice of magnonic spin torque and spin torques from thermoelectric current ($\acute{F}_m \geq 0$), and subsequently diffuse to the whole system with a gradient in the density, as indicated by the integrated probability for skyrmion distribution.

Electrical detection of thermally generated skyrmions

The presence of skyrmions could significantly affect the dynamics of conduction electrons[2,4]. One well known example is the anomalous Nernst effect (ANE)[15], in which the Nernst voltage reads as $V_{ANE} \propto M_z \cdot \Delta T(x)$, with M_z representing the change of perpendicular magnetization that is related to the change of total skyrmion number. This motivates the electrical detection of thermally generated skyrmions using the same type of device in Fig. 1A. Note that skyrmions contribute to the Nernst voltage through their magnetization (M_z) and its topology (Q). The skyrmion diffusion could also produce a topological Nernst voltage, but it is expected to be much smaller[35,36]. By referring to resistance-current (*R-I*) and temperature-resistance (*R-T*) curves of both heaters (H1,2), temperatures therein can be experimentally determined (labeled as $T_{1,2}^{M}$), which are consistent with our COMSOL simulation. The temperature differences between T_{U-E}^{S} and T_{L-E}^{S} thus determine the temperature gradients $\Delta T(x)$ across the multilayer, as shown in Figs. 4A and 4B. Under temperature gradients $\Delta T(x) = \pm 2.8\, K/\mu m$ generated by either the upper (H1) or the lower (H2) heater, opposite signs of voltages can be observed as shown in Fig. 4C. More ANE data can be found in the Extended Data S9.

At fixed $T(x)$ and constant $B_\perp$, the change of V_{ANE} reflects the change of magnetization and hence the total skyrmion numbers, as given in Fig. 4C. To demonstrate the electrical detection of a single skyrmion, we first applied a large current I = 6 mA ($T_{U-E}^{S} = 515\, K > T_{U-E}^{th}$) to generate skyrmions and kick off their diffusion. V_{ANE} was then measured under a smaller current I = 3 mA to maintain $\Delta T(x) = 0.9\, K/\mu m$, where no new

skyrmions were generated during the measurement [$(T^{S}_{U-E}(341\,K) < T^{th}_{U-E}(390\,K)$]. The time dependent V_{ANE} measured at $\mu_0 H_\perp = 25\,mT$ and the corresponding current pulse profile are displayed in Fig. 4D. Right after switching to current I = 3 mA, V_{ANE} decreases sharply, signifying the reduction of total skyrmion number and/or change in magnetization distribution. Interestingly, we observed many discretized steps in the time evolution of V_{ANE} where the change of V_{ANE} is discretized by $\Delta V_{ANE} = 90 \pm 10\,nV$. Each discretized jump can be naturally explained by the dissappearnce of a single skyrmion in the multilayer, which results in change of M_z when approaches the thermal equilibrium[37]. Compared to our micromagnetic simulations given in the Extended Data S8 and diffusion dynamics in Fig. 3A, we conclude that these discretized jumps $|V_{ANE}|$ correspond to the disappearance of a single skyrmion, likely through sample edges or structural defects in the interior of the device. Our experiments thus suggest that anomalous Nernst effect can be used for electrical detection of single skyrmion in similar multilayers[38].

Perspective

We have demonstrated the on-chip thermal generation, manipulation and detection of nanoscale skyrmions in metallic multilayers. Specifically, a unidirectional diffusion of skyrmions from the hot region toward the cold region is observed which can be attributed to combined contribution from the repulsive forces between skyrmions, the entropic force and thermal SOTs in competing with the magnonic spin torque. More importantly, discretized jumps in anomalous Nernst voltages were measured for electrical detection of a single skyrmion. Our experiments could serve as a complimentary approach that can be integrated with the existing electrical manipulation scheme, and can be extended for studying different types of topological spin textures in various ferromagnetic and ferroelectric materials[27,39-41]. In particular, insulating skyrmion-hosting materials where electrical currents are inapplicable, are perfect testing platforms[26,27]. Based on the Onsager reciprocal relation, the interacting thermal currents and skyrmion lattices could also result in many topological phenomena to be examined at room temperature, including the topological magnon Hall effect, and thermally induced skyrmion Hall effect, just to name a few examples[4,23]. Thus, the thermal generation, manipulation and detection of skyrmions could largely expand the current paradigm of

skyrmion spintronics, and may lead to skyrmionic, magnonic and spin caloritronic discoveries in the future.

Methods

Interfacially asymmetric magnetic multilayers of composition and stacking order $[Ta(30Å)/Co_{20}Fe_{60}B_{20}(11Å)/MgO(20Å)]_{15}$, $[Pt(20Å)/Co_{20}Fe_{60}B_{20}(11Å)/MgO(14Å)/Ta(10Å)]_{15}$ and $[Pt(15Å)/Co(10Å)/Ta(5Å)]_{15}$ were grown onto semi-insulating Si substrates covered with 300 nm thick thermally formed SiO_2 layer, and onto a 100 nm thick Si_3N_4 membrane on top of Si supporting frames. These films were made by using a dc magnetron sputtering system (AJA, Orion 8) at room temperature under Ar pressure 3 mTorr with a base pressure of the sputtering chamber $< 2 \times 10^{-8}$Torr. The Si_3N_4 membranes we used in this study are from CleanSiN (Suzhou). Multilayer channels on 100 nm thick Si_3N_4 membranes were first patterned by using electron beam lithography and followed by a lift-off process, which were annealed in vacuum for 30 minutes to induce the perpendicular magnetic anisotropy. Subsequently, Ta (20 nm)/Pt (50 nm) electrodes were deposited. A Quantum Design superconducting quantum interference device (SQUID) magnetometer was used to measure the magnetic properties. Damping parameters in multilayers were determined from ferromagnetic resonance (FMR). In order to probe the dominant out-of-plane X-ray magnetic circular dichroism (XMCD) contrast, samples on 100 nm thick Si_3N_4 membrane for XMCD imaging were positioned with the plane normal to the incident circularly polarized X-ray beam. The best magnetic contrast is obtained at Fe L_3 edge 708.5 eV for the $[Ta/Co_{20}Fe_{60}B_{20}/MgO]_{15}$ multilayers. The magnetic contrasts obtained at Co L_3 edge 778.5 eV for the $[Pt/Co_{20}Fe_{60}B_{20}/MgO/Ta]_{15}$ multilayers are relatively weak due to the less content of Co. Voltage pulses supplied into the on-chip heaters were provided by an Agilent 81150A arbitrary waveform generator and monitored with a 50 Ω terminated real time oscilloscope, through which the current flowing in the heater can be calculated. Note that for anomalous Nernst measurement, the length of the multilayer channel is 30 μm.

Calibration of temperatures of both heaters were made by firstly measuring the resistance change of heaters as a function of current/voltage, through comparing with temperature dependent resistance change, temperatures at both heaters can be identified. The presence of temperature gradients is further confirmed through anomalous Nernst

measurement. The presence of approximately linear temperature gradients in the sample are also experimentally verified, and discussed in the Part 8 of the Supplementary Materials. Temperature profiles of the devices were simulated by using COMSOL Multiphysics software. We implemented a conjoint *Joule Heating* module, which includes the *AC/DC* module to apply the pulse voltages. A *Heat Transfer* module was used to describe the heat flow and temperature distribution. Since the most part of the device is located on top of the 500 μm × 500 μm SiN (100 nm), we therefore limited our simulation in this area. For heaters and electrodes, the materials parameters for Pt are used: thickness of 70 nm and an electrical conductivity of 8.9×10^6 S/m. The multilayer channels were simplified as: $[Ta(15nm)/Co_{20}Fe_{60}B_{20}(5.5nm)/MgO(10nm)]_3$, $[Pt(10nm)/Co_{20}Fe_{60}B_{20}(5.5nm)/MgO(9nm)/Ta(5nm)]_3$ and $[Pt(7.5nm)/Co(5nm)/Ta(2.5nm)]_5$, to save the simulation time. All parameters including density ρ, specific heat capacity C_ρ, thermal conductivity κ and electrical conductivity σ and thermal expansion coefficient L used in COMSOL simulations are shown in Table S1 in the Supplementary Materials. We used the fixed boundary condition with temperature fixed at 293 K.

Micromagnetic simulation studies were independently carried out using a home-built code and by using a state-of-the-art micromagnetic solver, PETASPIN, full description which can be found in the Supplementary Materials.

Acknowledgements

Work carried out at Tsinghua was supported by the Basic Science Center Project of NSFC (Grant No. 51788104), the National Key R&D Program of China (Grant Nos. 2017YFA0206200 and 2016YFA0302300), the National Natural Science Foundation of China (Grant No. 11774194, 51831005, 1181101082, 11804182), Beijing Natural Science Foundation (Grant No. Z190009), Tsinghua University Initiative Scientific Research Program and the Beijing Advanced Innovation Center for Future Chip (ICFC). The work at LANL was carried out under the auspices of the U.S. DOE NNSA under contract No. 89233218CNA000001 through the LDRD Program, and was supported by the Center for Nonlinear Studies at LANL. Works at the ALS were supported by U.S. Department of Energy (DE-AC02-05CH11231). M.-Y. Im acknowledges support from the National Research Foundation (NRF) of Korea funded by the Ministry of Education, Science and ICT (2018K1A4A3A03075584, 2016M3D1A1027831), DGIST R&D program of the Ministry of

Science, ICT and future Planning (18-BT-02) and support by Lawrence Berkeley National Laboratory through the Laboratory Directed Research and Development (LDRD) Program. R.T. and G.F. thank the project "ThunderSKY" funded from the Hellenic Foundation for Research and Innovation (HFRI) and the General Secretariat for Research and Technology (GSRT) under Grant No. 871. Authors wish to thank Naoto Nagaosa, Markus Garst, Jiadong Zang, Guoqiang Yu and Yayu Wang for fruitful discussions.

Author contributions

W.J. conceived the idea and designed the experiments. H.Z. and T.X. fabricated the thin film. Z.W., H.Z., L.Z., Y.D. and C.S. performed lithographic processing. Z.W. and K.W. did the COMSOL simulation. M.G., H.B. and H.W. did the thermoelectric measurements. Y.Y., H.Z. and W.H. carried out ferromagnetic resonance experiments. S.L. performed atomistic micromagnetic simulation and Fokker-Planck calculation. R.T. performed the layer dependent micromagnetic simulations. R.T. and G. F. analyzed the micromagnetic simulation data. M.C and G.F. implemented the micromagnetic solver for multilayer calculations. Z.W., S.J., H.H., K.L., S.L., W.C., M.I and W.J. performed the full field soft X-ray microscope imaging experiments and data analysis. W.J. and S.L. wrote the manuscript with inputs from all authors.

Additional information.

Supplementary information is available in the online version of the paper. Preprints and permission information is available online at www.nature.com/reprints. Correspondence and requests for materials should be addressed to S.L. and W.J.

Competing financial interests

Authors declare no competing financial interests.

References

1 Yu, X. Z. *et al.* Real-space observation of a two-dimensional skyrmion crystal. *Nature* **465**, 901-904 (2010).

2 Jonietz, F. *et al.* Spin transfer torques in MnSi at ultralow current densities. *Science* **330**, 1648-1651 (2010).

3 Fert, A., Cros, V. & Sampaio, J. Skyrmions on the track. *Nature Nanotechnology* **8**, 152-156 (2013).
4 Nagaosa, N. & Tokura, Y. Topological properties and dynamics of magnetic skyrmions. *Nature Nanotechnology* **8**, 899-911 (2013).
5 Bogdanov, A. N. & Rößler, U. K. Chiral symmetry breaking in magnetic thin films and multilayers. *Physical Review Letters* **87**, 037203 (2001).
6 Heinze, S. *et al.* Spontaneous atomic-scale magnetic skyrmion lattice in two dimensions. *Nature Physics* **7**, 713-718 (2011).
7 Romming, N. *et al.* Writing and deleting single magnetic skyrmions. *Science* **341**, 636-639 (2013).
8 Jiang, W. *et al.* Blowing magnetic skyrmion bubbles. *Science* **349**, 283-286 (2015).
9 Chen, G., Mascaraque, A., N'Diaye, A. T. & Schmid, A. K. Room temperature skyrmion ground state stabilized through interlayer exchange coupling. *Appl Phys Lett* **106**, 242404 (2015).
10 Woo, S. *et al.* Observation of room-temperature magnetic skyrmions and their current-driven dynamics in ultrathin metallic ferromagnets. *Nature Materials* **15**, 501-506 (2016).
11 Moreau-Luchaire, C. *et al.* Additive interfacial chiral interaction in multilayers for stabilization of small individual skyrmions at room temperature. *Nature Nanotechnology* **11**, 444-448 (2016).
12 Fert, A., Reyren, N. & Cros, V. Magnetic skyrmions: advances in physics and potential applications. *Nat Rev Mater* **2**, 17031 (2017).
13 Everschor-Sitte, K., Masell, J., Reeve, R. M. & Klaui, M. Perspective: Magnetic skyrmions-Overview of recent progress in an active research field. *Journal of Applied Physics* **124**, 240901 (2018).
14 Jakub Zázvorka *et al.* Thermal skyrmion diffusion used in a reshuffler device. *Nature Nanotechnology* **14**, 658-661 (2019).
15 Bauer, G. E. W., Saitoh, E. & van Wees, B. J. Spin caloritronics. *Nature Materials* **11**, 391-399 (2012).
16 Koshibae, W. & Nagaosa, N. Creation of skyrmions and antiskyrmions by local heating. *Nature Communications* **5**, 5148 (2014).
17 Lin, S. Z., Batista, C. D., Reichhardt, C. & Saxena, A. ac Current Generation in Chiral Magnetic Insulators and Skyrmion Motion induced by the Spin Seebeck Effect. *Physical Review Letters* **112**, 187203 (2014).
18 Kovalev, A. A. & Tserkovnyak, Y. Thermoelectric spin transfer in textured magnets. *Physical Review B* **80**, 100408 (2009).
19 Everschor, K. *et al.* Rotating skyrmion lattices by spin torques and field or temperature gradients. *Physical Review B* **86**, 054432 (2012).
20 Kong, L. Y. & Zang, J. D. Dynamics of an Insulating Skyrmion under a Temperature Gradient. *Physical Review Letters* **111**, 067203 (2013).
21 Mochizuki, M. *et al.* Thermally driven ratchet motion of a skyrmion microcrystal and topological magnon Hall effect. *Nature Materials* **13**, 241-246 (2014).
22 Wild, J. *et al.* Entropy-limited topological protection of skyrmions. *Science Advances* **3**, e1701704 (2017).
23 Shiomi, Y., Kanazawa, N., Shibata, K., Onose, Y. & Tokura, Y. Topological Nernst effect in a three-dimensional skyrmion-lattice phase. *Physical Review B* **88**, 064409 (2013).

24 Chumak, A. V., Vasyuchka, V. I., Serga, A. A. & Hillebrands, B. Magnon spintronics. *Nature Physics* **11**, 453-461 (2015).
25 R. Tomasello *et al.* A strategy for the design of skyrmion racetrack memories. *Scientific Reports* **4**, 6784 (2014).
26 Seki, S., Yu, X. Z., Ishiwata, S. & Tokura, Y. Observation of Skyrmions in a Multiferroic Material. *Science* **336**, 198-201 (2012).
27 Kézsmárki, I. *et al.* Néel-type skyrmion lattice with confined orientation in the polar magnetic semiconductor GaV4S8. *Nature Materials* **14**, 1116 (2015).
28 Lemesh, I. *et al.* Current-Induced Skyrmion Generation through Morphological Thermal Transitions in Chiral Ferromagnetic Heterostructures. *Advanced Materials* **30**, 1805461 (2018).
29 Muller, J., Rosch, A. & Garst, M. Edge instabilities and skyrmion creation in magnetic layers. *New Journal of Physics* **18**, 065006 (2016).
30 Bottcher, M., Heinze, S., Egorov, S., Sinova, J. & Dupe, B. B-T phase diagram of Pd/Fe/Ir(111) computed with parallel tempering Monte Carlo. *New Journal of Physics* **20**, 103014 (2018).
31 Zhang, X. C. *et al.* Skyrmion-skyrmion and skyrmion-edge repulsions in skyrmion-based racetrack memory. *Scientific Reports* **5**, 7643 (2015).
32 Rohart, S. & Thiaville, A. Skyrmion confinement in ultrathin film nanostructures in the presence of Dzyaloshinskii-Moriya interaction. *Physical Review B* **88**, 184422 (2013).
33 Bessarab, P. F. *et al.* Lifetime of racetrack skyrmions. *Scientific Reports* **8**, 3433 (2018).
34 Lin, S.-Z. Edge instability in a chiral stripe domain under an electric current and skyrmion generation. *Physical Review B* **94**, 020402(R) (2016).
35 Zeissler, K. *et al.* Discrete Hall resistivity contribution from Neel skyrmions in multilayer nanodiscs. *Nature Nanotechnology* **13**, 1161-1166 (2018).
36 Maccariello, D. *et al.* Electrical detection of single magnetic skyrmions in metallic multilayers at room temperature. *Nature Nanotechnology* **13**, 233-237 (2018).
37 Kanazawa, N. *et al.* Discretized topological Hall effect emerging from skyrmions in constricted geometry. *Physical Review B* **91**, 041122 (2015).
38 Scarioni, A. F. *et al.* (Preprint at: https://arxiv.org/pdf/2001.10251., 2020).
39 Nayak, A. K. *et al.* Magnetic antiskyrmions above room temperature in tetragonal Heusler materials. *Nature* **548**, 561 (2017).
40 Yu, X. Z. *et al.* Transformation between meron and skyrmion topological spin textures in a chiral magnet. *Nature* **564**, 95-98 (2018).
41 Das, S. *et al.* Observation of room-temperature polar skyrmions. *Nature* **568**, 368-372 (2019).

Figure Captions

Figure 1. Thermal generation of skyrmions via using on-chip heaters. Fig. A is an optical image of the integrated device with two identical Ta/Pt heaters on top of a 100 nm thick Si_3N_4 membrane. The imaging area is marked as a blue circle in the center of the $[Ta/CoFeB/MgO]_{15}$ multilayer channel. The computed temperature profile is shown in the left upper panel of Fig. B with a pulse voltage of amplitude V_h=¿0.59 V and duration 100 μs. Shown in the left lower panel of Fig. B is a linescan of temperature profile (cyan line) from which a linear temperature gradient in the multilayer can be found. Temperatures of both heaters ($T^S_{H1,2}$) and the upper and the lower edges of the multilayer channel were computed and labeled as T^S_{U-E} and T^S_{L-E}, respectively. Shown in Figs. C and D are the transformation from the original stripe domains into densely packed skyrmions after applying a pulse voltage of duration 100 μs and amplitude V_h=¿0.59 V to the upper heater (H1) for negative magnetic field ($\mu_0 H_\perp = -$¿25.6 mT) and positive field ($\mu_0 H_\perp = +$¿25.4 mT), respectively. White color corresponds to magnetization downward while black color denotes magnetization upward, respectively.

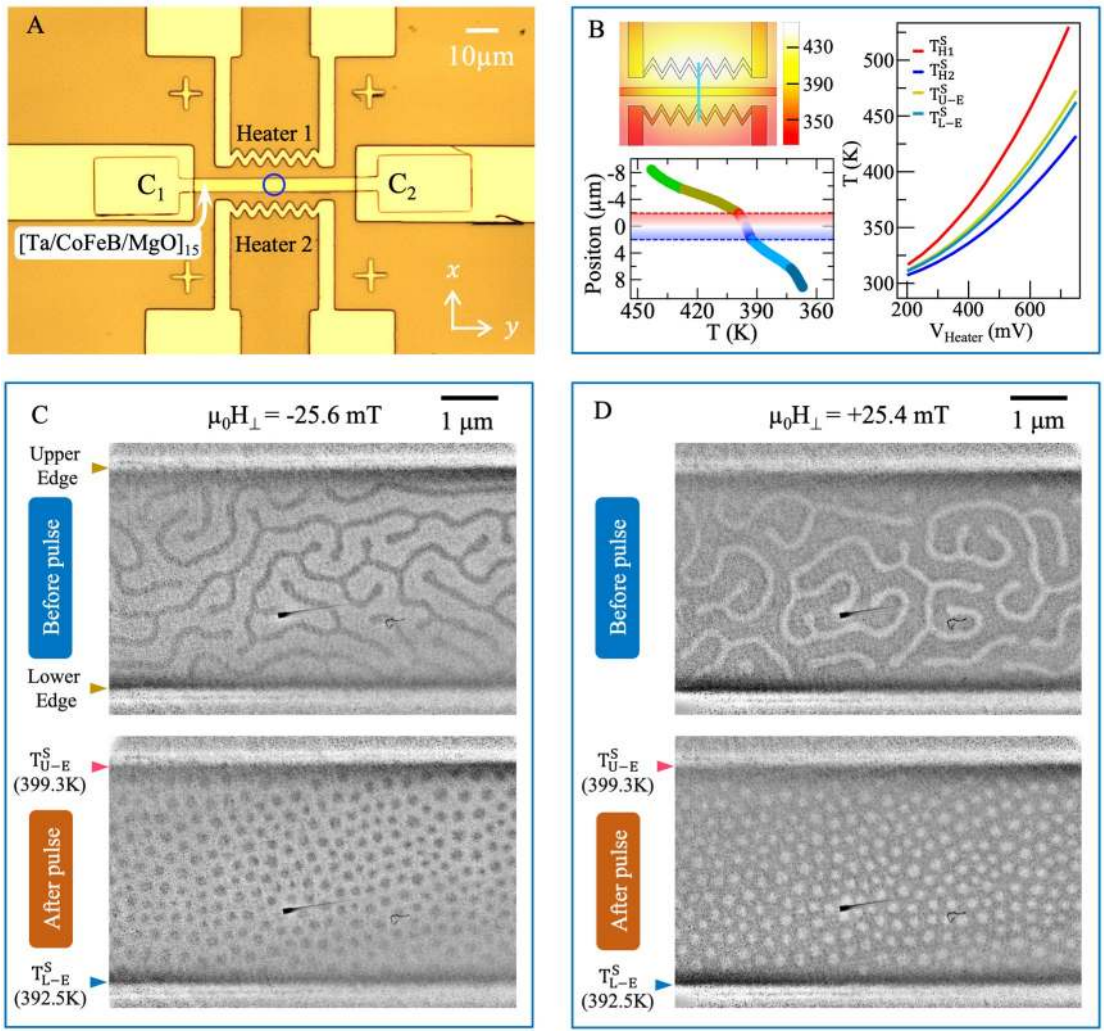

Figure 2. Transformational dynamics and phase diagram in different multilayers. Shown in Figs. A and B are consecutive images acquired in the $[Ta/CoFeB/MgO]_{15}$ multilayer at $\mu_0 H_\perp = -¿19.3$ mT and $\mu_0 H_\perp = -¿27.6$ mT, before and after applying pulse voltages (duration fixed at 100 μs) into the upper heater (H1), in which the computed temperatures at the hot side (T^S_{U-E}) can also be found. Shown in Fig. A are images taken before and after applying the following pulse voltages into the heater: $V_h = ¿0.514$ V(1^{st}), $V_h = ¿0.517$ V(2^{nd}), $V_h = ¿0.525$ V(3^{rd}) and $V_h = ¿0.531$ V(4^{th}) at $\mu_0 H_\perp = -¿19.3$ mT. Shown in Fig. B are images taken after applying $V_h = ¿0.556$ V(1^{st}), $V_h = ¿0.560$ V(2^{nd}), $V_h = ¿0.571$ V(3^{rd}) and $V_h = ¿0.586$ V(4^{th}) at $\mu_0 H_\perp = -¿27.6$ mT. While domains are absent from the original image, skyrmions and stripe domains can also be generated. In the $[Pt/Co/Ta]_{15}$ multilayers, skyrmions can be similarly generated from the hot edge ($436\,K < T^S_{U-E} < 464\,K$), which then propagate from the hot side towards the cold side followed by the growing area of skyrmion lattices, as shown in Fig. C. The amplitude of voltages (100 μs) at the hot edges are: $V_h = ¿0.682$ V(1^{st}), $V_h = ¿0.701$V(2^{nd}), $V_h = ¿0.712$ V(3^{rd}) and $V_h = ¿0.745$ V(4^{th}). Shown in Fig. 2D is the dependence of the threshold skyrmion generation temperatures (T^{th}_{U-E}) on the damping parameters (α) at $\mu_0 H_\perp = 25.4$ mT. Fig. E corresponds to the skyrmion generation rate as a function of T^S_{U-E} for the $[Ta/CoFeB/MgO]_{15}$ multilayer. A phase diagram summarizing the evolution of different magnetic phases as a function of T^S_{U-E} and $\mu_0 H_\perp$ is constructed in Fig. F for the $[Ta/CoFeB/MgO]_{15}$ multilayer.

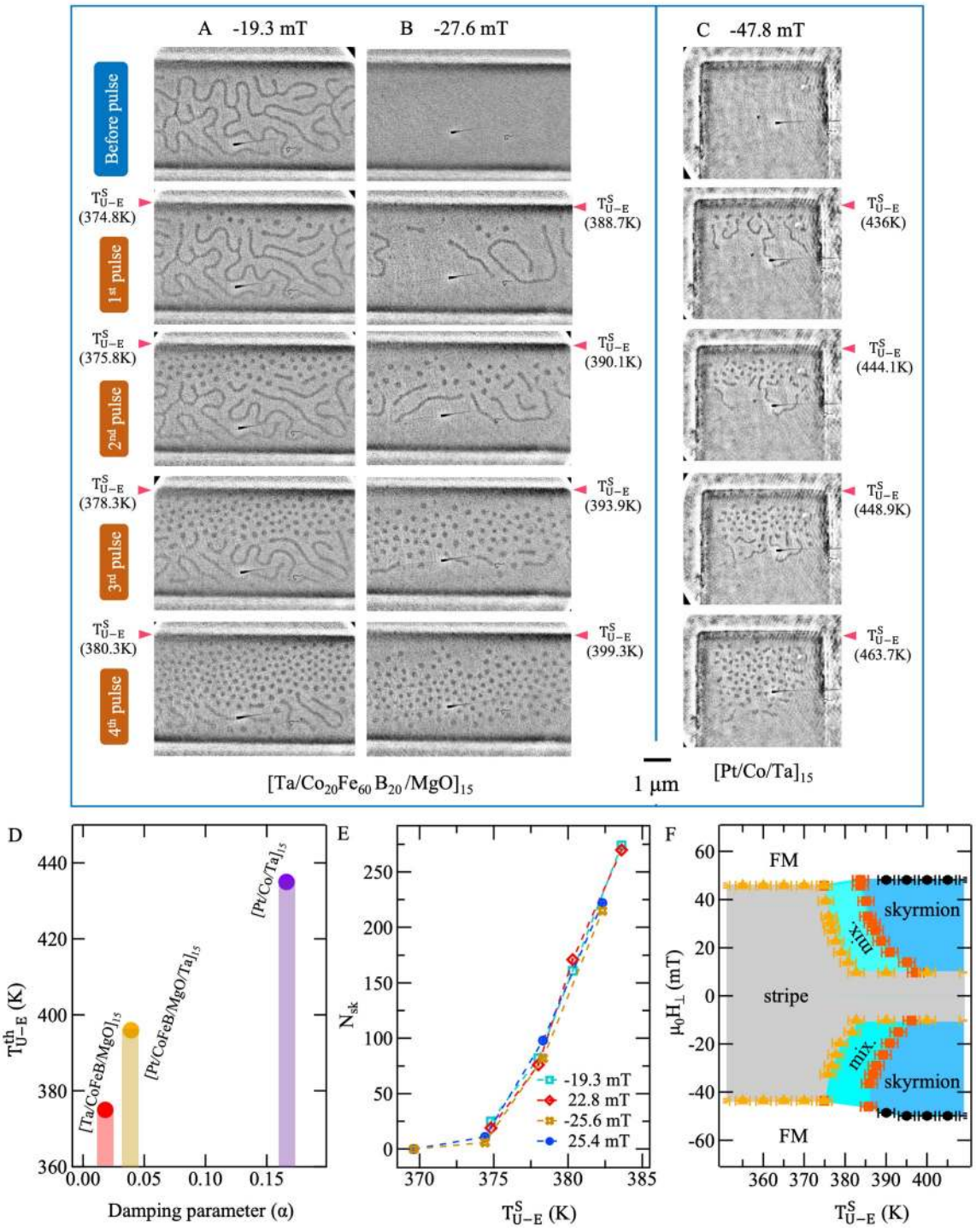
A -19.3 mT
B -27.6 mT
C -47.8 mT
Before pulse
1st pulse
2nd pulse
3rd pulse
4th pulse
T^S_{U-E} (374.8K)
T^S_{U-E} (388.7K)
T^S_{U-E} (436K)
T^S_{U-E} (375.8K)
T^S_{U-E} (390.1K)
T^S_{U-E} (444.1K)
T^S_{U-E} (378.3K)
T^S_{U-E} (393.9K)
T^S_{U-E} (448.9K)
T^S_{U-E} (380.3K)
T^S_{U-E} (399.3K)
T^S_{U-E} (463.7K)
$[Ta/Co_{20}Fe_{60}B_{20}/MgO]_{15}$
1 μm
$[Pt/Co/Ta]_{15}$
D
T^{th}_{U-E} (K)
Damping parameter (α)
$[Ta/CoFeB/MgO]_{15}$
$[Pt/CoFeB/MgO/Ta]_{15}$
$[Pt/Co/Ta]_{15}$
E
N_{sk}
T^S_{U-E} (K)
-19.3 mT
22.8 mT
-25.6 mT
25.4 mT
F
$\mu_0 H_\perp$ (mT)
T^S_{U-E} (K)
FM
skyrmion
mix.
stripe
mix.
skyrmion
FM

Figure 3. Experimental demonstration of thermally induced skyrmion diffusion and analytical understandings of skyrmion generation and diffusion. Show in Fig. A-1 is a scanning electron microscope image. Following the increased temperature gradients (duration is fixed at 500 ms), a unidirectional diffusion of skyrmions from the hot region towards the cold region is observed in a device with a sharp tip in the $[Ta/CoFeB/MgO]_{15}$ multilayer, as shown in Figs. A2-A7. Summarized in Figs. A-8 and A-9 are the diffusion trajectory and the velocity of the selected skyrmions. Marked in the purple hexagon is a pinned skyrmion. Micromagnetic simulation results are shown in Fig. B. Following the increasing number of frames (P_0, P_6, P_{23}, P_{53}, P_{98}), skyrmions are first nucleated at the hot edge, followed by a directional motion from the hot region towards the cold region. The time lapse between consecutive frames is $\Delta t = 120 J_{ex}/\gamma D^2$. The coefficient of temperature gradient is $k = 0.01 J_{ex}/k_B$. The film thickness is $0.1 J_{ex}/D$. The scale bar is $20 J_{ex}/D$. The integrated skyrmion probability ($\acute{P}$) distribution as a function of position (J_{ex}/D) at different time (t) obtained by solving the Fokker-Planck equation are shown, (C) for a drift velocity $\acute{F}_m = 0.2$, (D)$\acute{F}_m$ ¿0, respectively. In the calculations, we use the absorbing boundary condition at $x = 0$ by setting $\acute{P}(x=0)=0$ at the cold side and $\partial_x \acute{P}(x=L_x)=0$ at the hot side. The length is in unit of J_{ex}/D and time is in unit of by $4\pi d/\gamma D$.

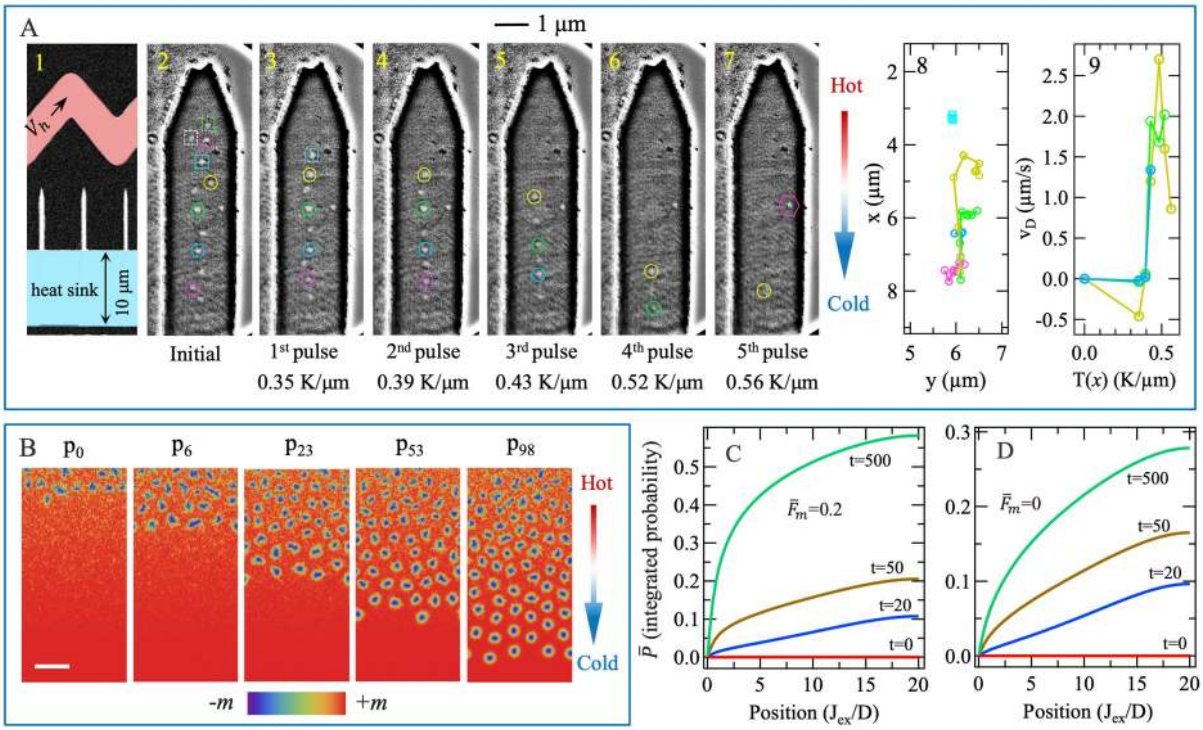

Figure 4. Electrical detection of skyrmions via the anomalous Nernst effect. Combined with COMSOL simulation and experimental measurements, temperatures and the accompanied temperature gradients $\Delta T(x)$ in the device are determined and shown in Figs. A and B, respectively. The simulated (line)/measured (dot) temperatures of both heaters are accordingly labeled as $T^{S}_{1,2}/T^{M}_{1,2}$. The opposite anomalous Nernst voltages (V_{ANE}) measured with the opposite temperature gradients [$\Delta T(x) = \pm 2.8\,K/\mu m$¿ are shown in Fig. C. At $\mu_0 H_\perp = 25$ mT, after switching off I = 6 mA, a smaller current I = 3 mA that generates $\Delta T(x) = 0.9\,K/\mu m$ is applied to measure the time evolution of V_{ANE}, in which several "quantized" jumps with $\Delta V_{ANE} = 90 \pm 10\,nV$ can be found. After saturating the sample above $\mu_0 H_\perp = 500$ mT and reducing the field back to $\mu_0 H_\perp =$¿25 mT, V_{ANE} falls back to the same value as before applying I = 6 mA in which the "quantized" jumps are absent.

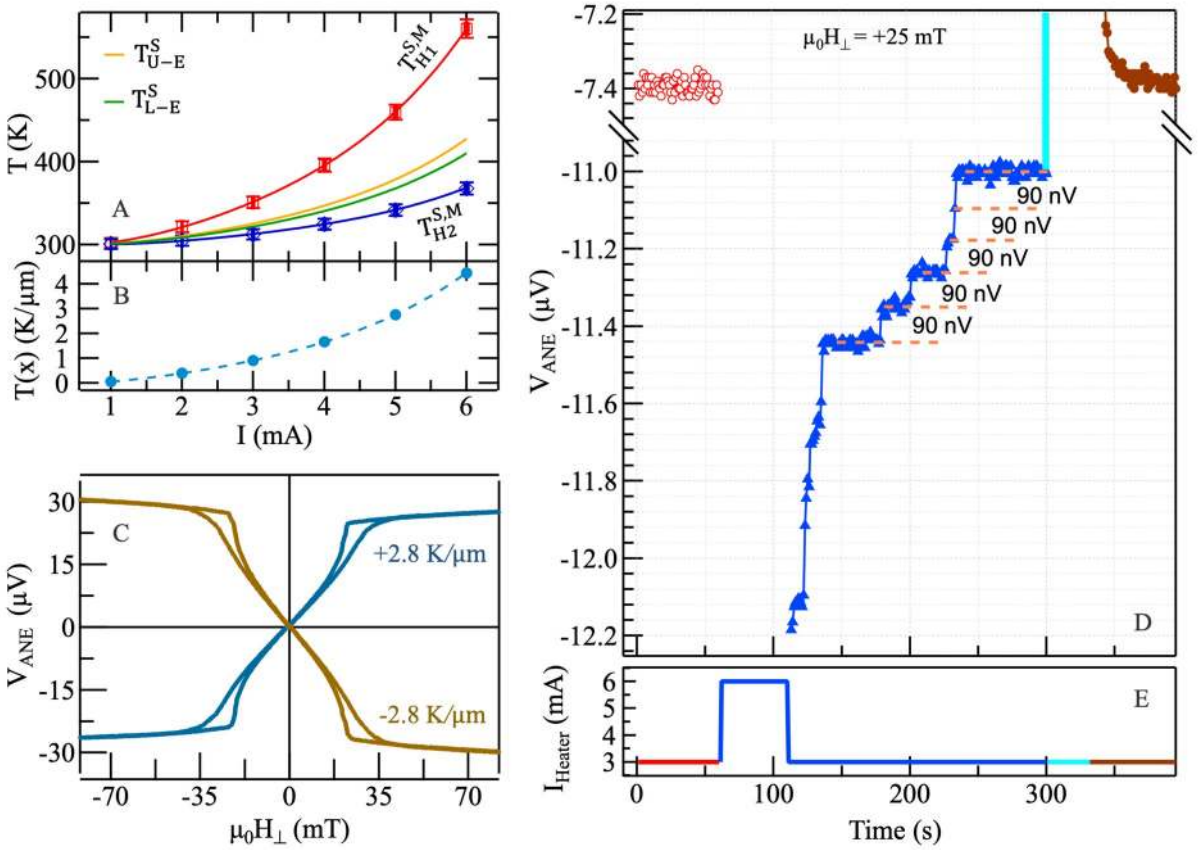

Extended Data S1. Skyrmion generations and propagation in the [Ta/$Co_{20}Fe_{60}B_{20}$/MgO]$_{15}$ multilayer at positive magnetic fields (+$\mu_0 H_\perp$) by using the upper heater. At different positive magnetic fields, by applying pulse voltages (duration fixed at 100 μs) into the upper heater (H1), the thermal generation of skyrmions, together with the propagation towards the cold side are evident. The experimentally utilized parameters and the estimated temperatures at the upper edge (hot side) are also listed.

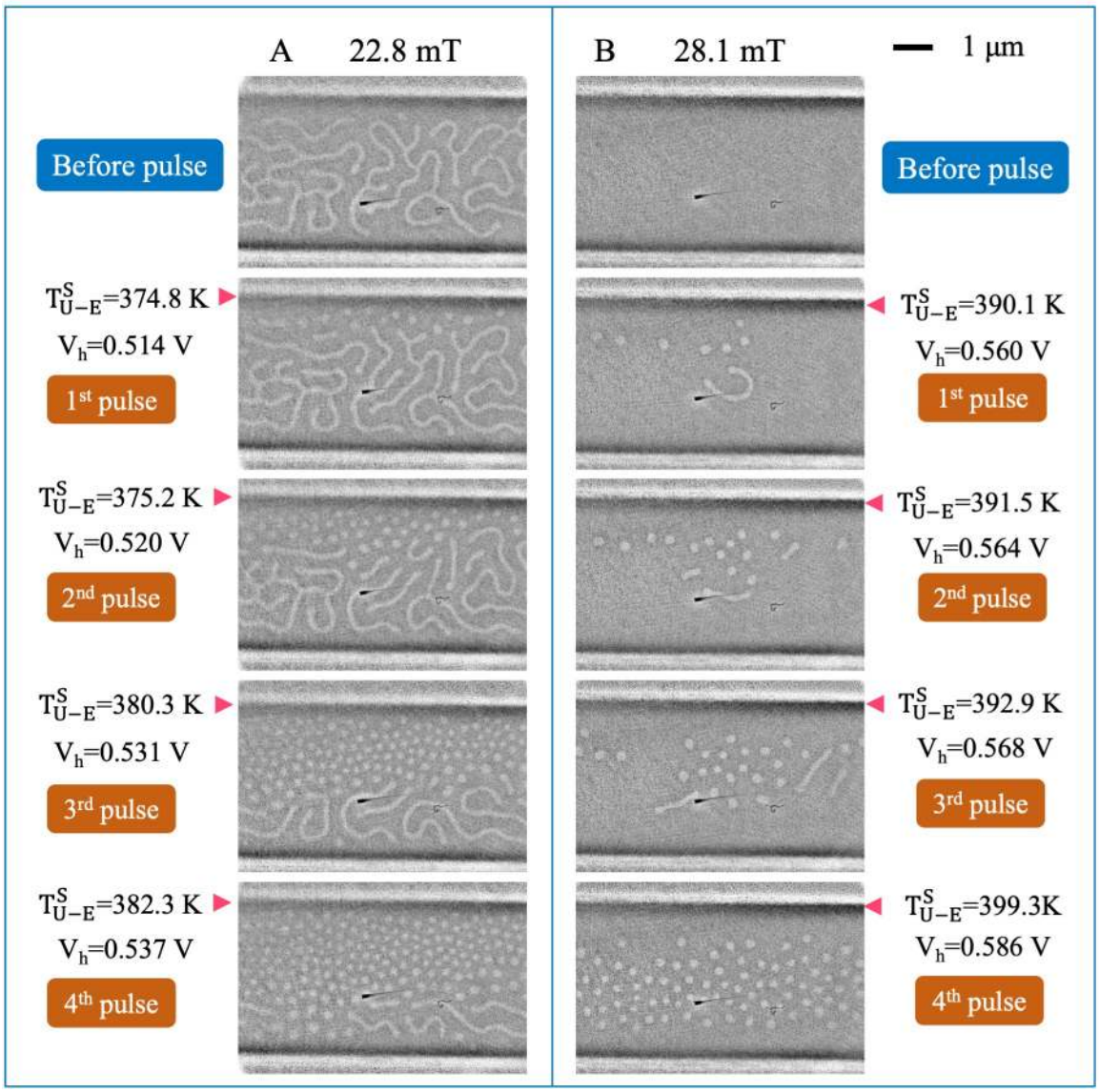

Extended Data S2. Morphological transition of stripe domains in the $[Ta/Co_{20}Fe_{60}B_{20}/MgO]_{15}$ multilayer at smaller magnetic fields by using the upper heater. At smaller (positive/negative) magnetic fields and by applying pulse voltages (duration fixed at 100 μs) into the upper heater, thermally induced morphological transition were observed.

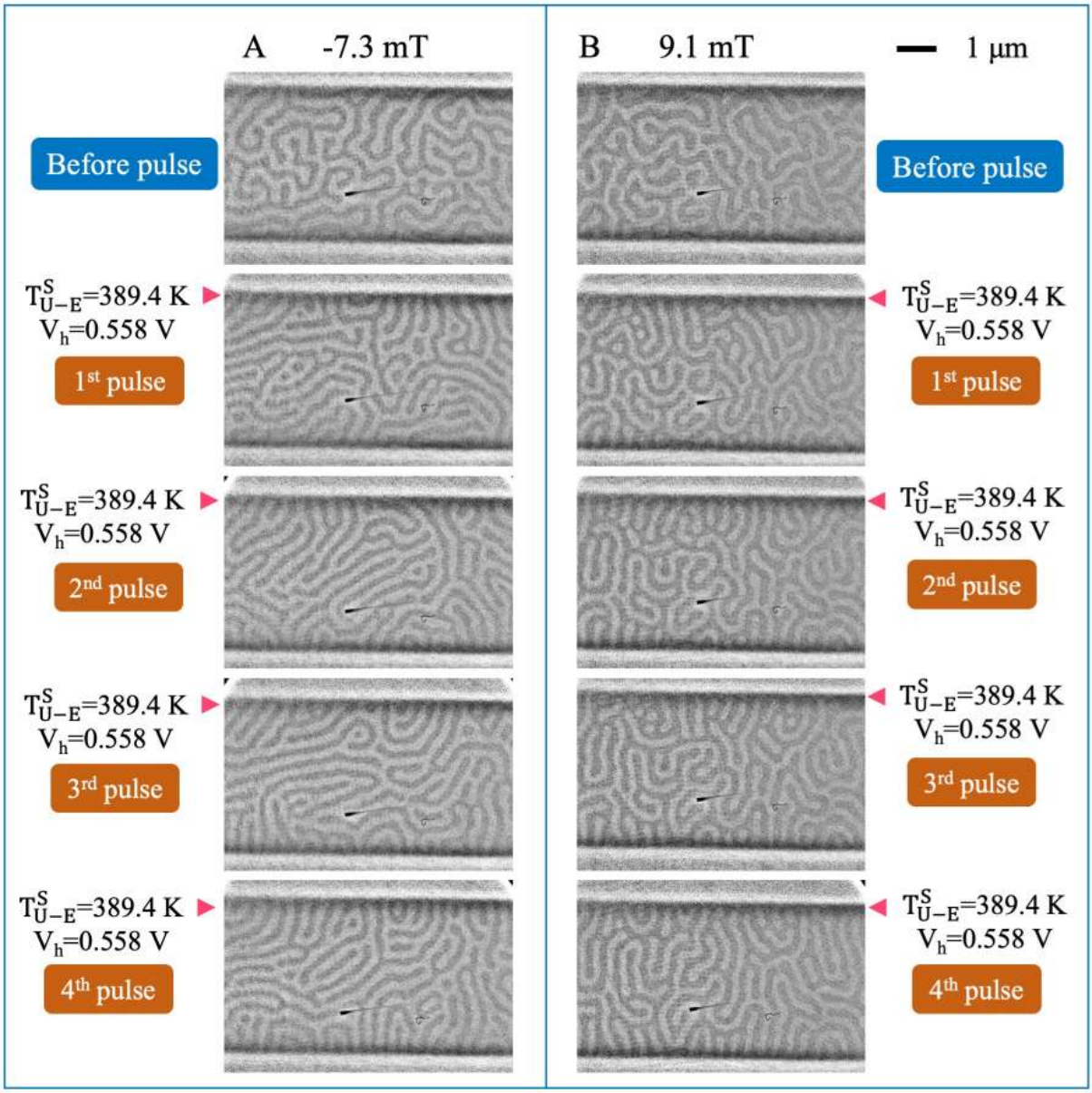

Extended Data S3. Skyrmion generation and propagation in the [Ta/$Co_{20}Fe_{60}B_{20}$/MgO]$_{15}$ multilayer by changing the pulse duration via the upper heater. By increasing the duration of pulse voltages (amplitude is fixed at V_h= ¿ 0.526 V) in the upper heater, thermal generation of skyrmion and skyrmion propagation towards the cold side (lower edge) were observed.

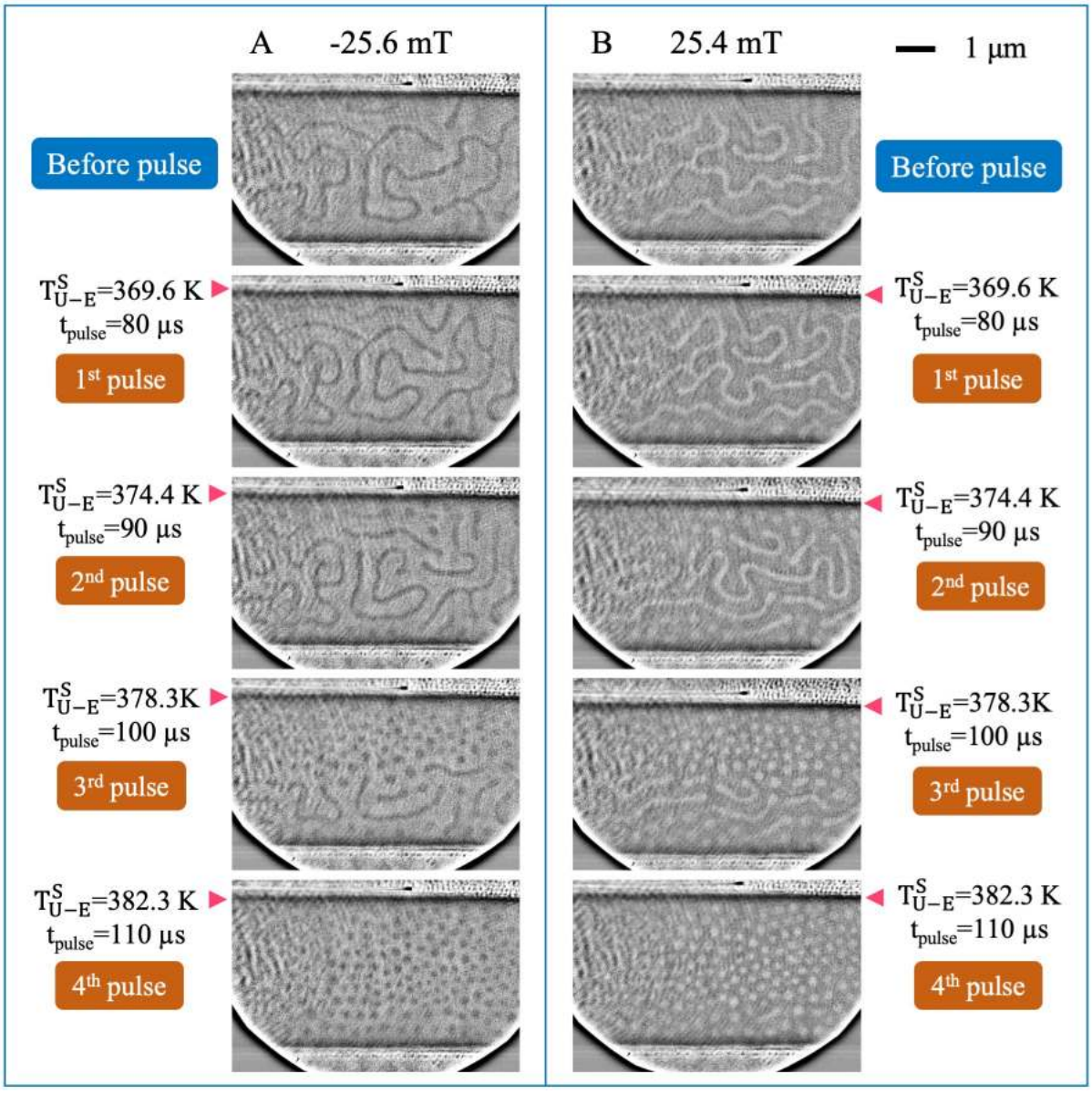

Extended Data S4. Skyrmion generations and propagation in the $[Ta/Co_{20}Fe_{60}B_{20}/MgO]_{15}$ multilayer by using the lower heater. At opposite magnetic fields, by applying pulse voltages (duration fixed at 100 μs) into the lower heater (H2), thermal generation of skyrmions, together with the propagation towards the cold side (upper side) were realized.

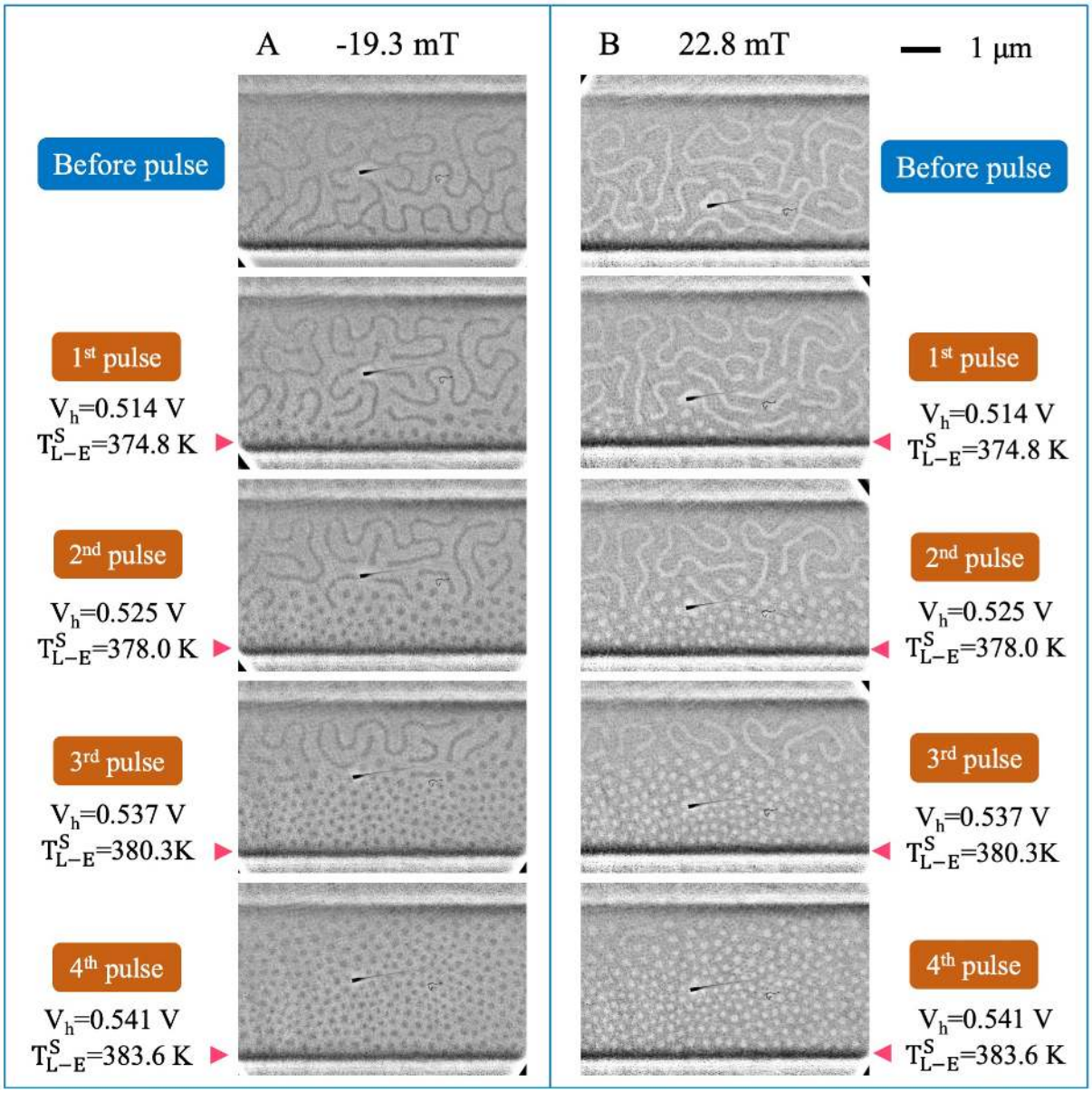

Extended Data S5. Skyrmion generations and propagation in the $[Pt/Co_{20}Fe_{60}B_{20}/MgO/Ta]_{15}$ multilayer by using the upper heater. At opposite magnetic fields, by applying increased amplitudes of pulse voltages (duration fixed at 100 μs) into the upper heater, thermal generation of skyrmions, together with the propagation towards the cold side were realized.

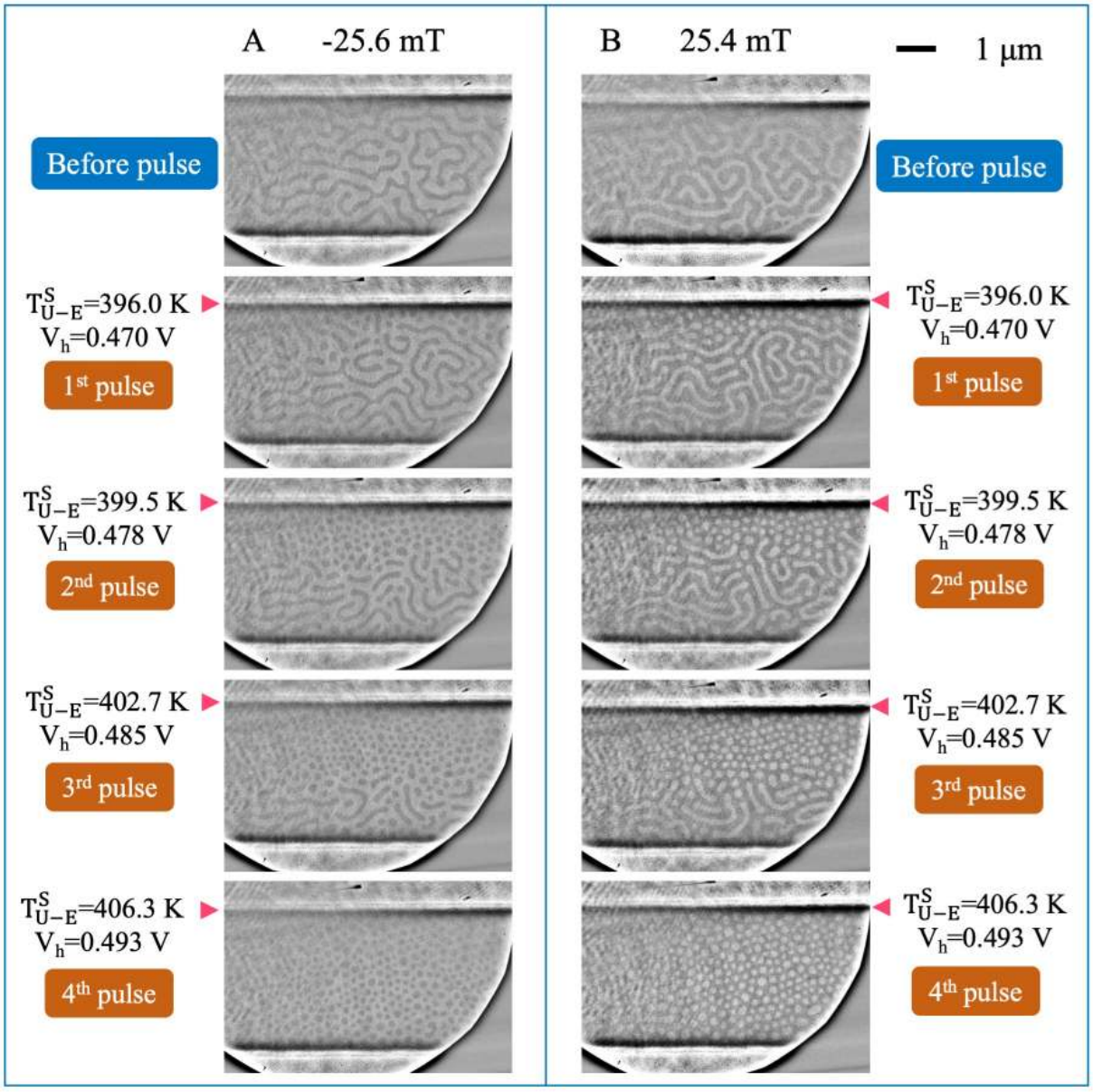

Extended Data S6. The phase diagram of skyrmion generation at different pulse durations in the [Ta/$Co_{20}Fe_{60}B_{20}$/MgO]$_{15}$ multilayer. Shown in (A) is the response of competing magnetic phase to different pulse duration (with a fixed amplitude V_h = 0.526 V) and magnetic fields. Shown in (B) is the dependence of the maximum temperatures at the upper (hot) edge (T^S_{U-E}) on the pulse duration (t_{pulse}), in which a nonlinear increase of T^S_{U-E} following the increase of pulse duration is observed, that can be attributed to the fast dissipation of heat through substrate. Following the continuous increase of pulse duration above 4 ms , the system approaches thermal equillibrium with a constant tempeature at the hot edge ($T^S_{U-E}=496\,K$), and a constant temperature gradient in the multiayer $\Delta T(x)=1.3\,K/\mu m$, as shown in Figs. (C) and (D), respectively.

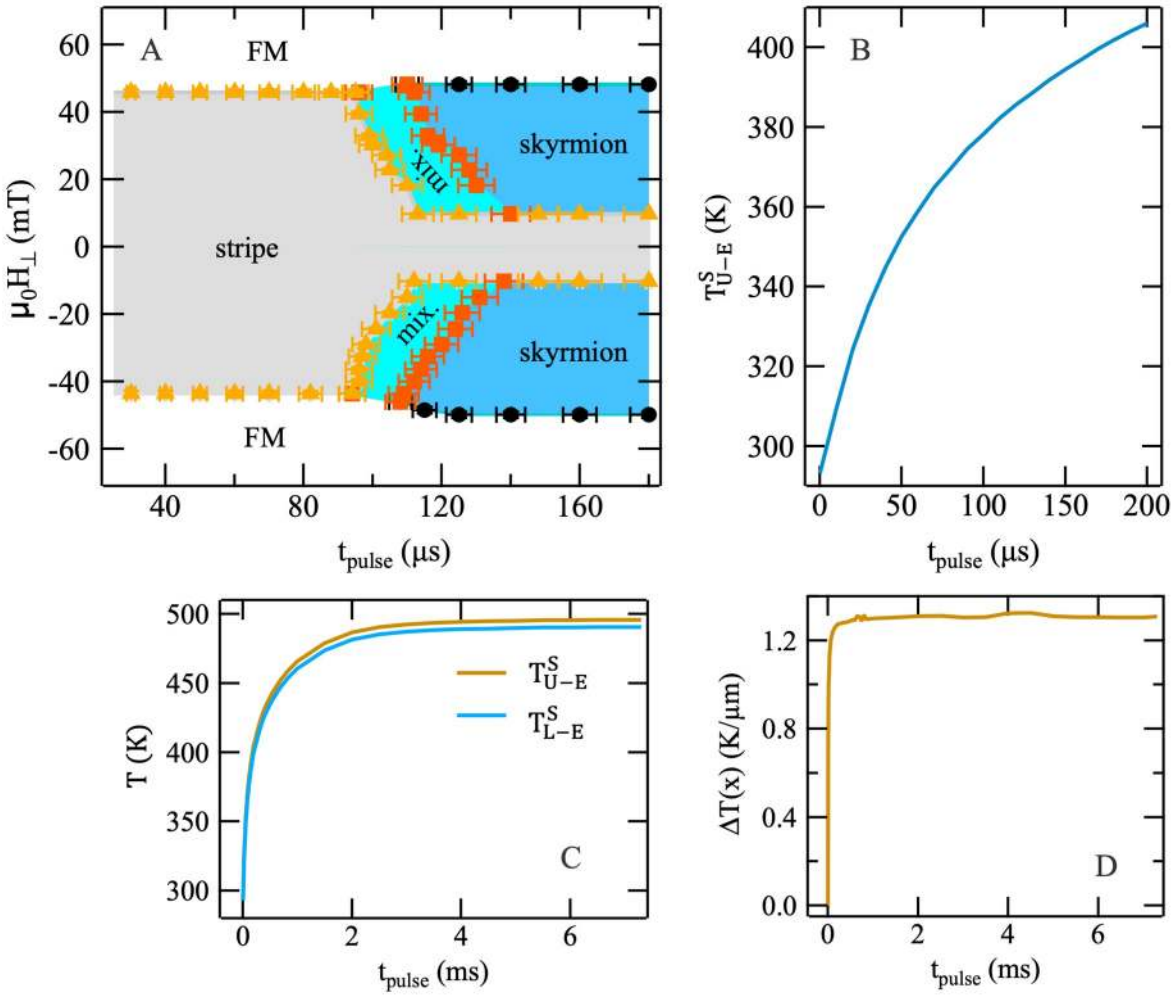

Extended Data S7. Micromagnetic simulation results of transformation from stripe domains to densely packed skyrmion lattices driven by temperature gradients. Following the increasing time, presented as number of frames (1, 30, 100, 200, 300, 400), skyrmions are first nucleated at the hot edge, followed by the immediate thermal diffusion from the hot side towards the cold side. Meanwhile, skyrmions are also generated by breaking the stripe domains followed by relaxation in the hot side. The diffusion of skyrmions then pushes the stripe domains out of the simulation box. The time lapse between consecutive frames is $\Delta t = 60 J_{ex}/\gamma D^2$. The temperature gradient is $k = 0.01 J_{ex}/k_B$ and $H_a = 0.6 D^2/J_{ex}$. Here we assume the film thickness is $0.1 J_{ex}/D$. The scale bar is $20 J_{ex}/D$. The open (periodic) boundary condition is used in the horizontal (vertical) direction.

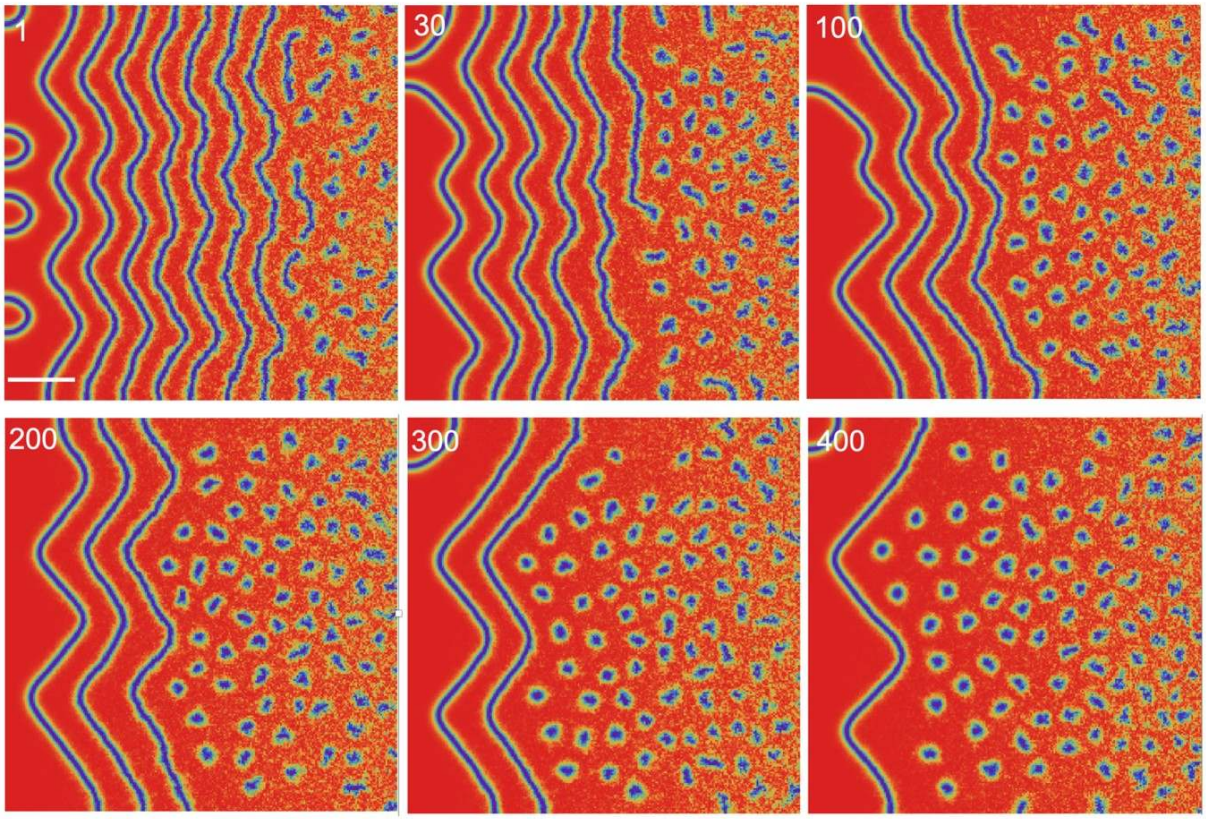

Extended Data S8. Micromagnetic simulation results of the diffusion of skyrmions purely driven by temperature gradients. We performed micromagnetic simulation of skyrmion diffusion in a nanowire geometry by using the open boundary condition. First, we thermally excite skyrmions at high temperature side using a larger temperature gradient. We subsequently reduce the temperature gradient to avoid the nucleation of skyrmions at the hot side, which results in the diffusion of skyrmions towards the cold side. Some skyrmions exit the nanowire through the sample edge during the diffusion. The length and the width of the nanowire are $120J_{ex}/D$ and $40J_{ex}/D$ respectively. The thermal gradient for diffusion is $k=0.008\,J_{ex}/k_B$. Disorders in spin anisotropy are introduced to suppress the magnonic spin torque by reducing the magnon mean free path. Here we assume the film thickness is $0.1\,J_{ex}/D$. The scale bar is $10J_{ex}/D$.

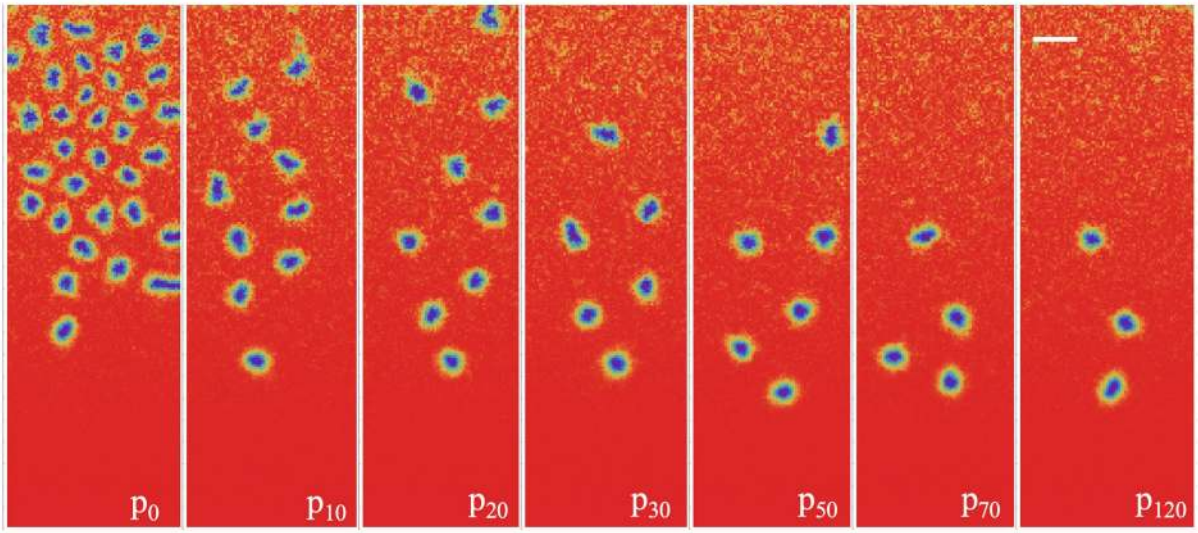

Extended Data S9. Anomalous Nernst effect measured under different temperature gradients in the [Ta/$Co_{20}Fe_{60}B_{20}$/MgO]$_{15}$ multilayer. Shown in (A) is the evolution of anomalous Nernst voltages (V_{ANE}) measured with different current supplied into the heater (I_{Heater}). Following the increase of I_{Heater}, a parabolic increase of saturated $V_{ANE}(\mu_0 H_\perp = 100\,mT)$ can be found and summarized in (B). The evolution of $V_{ANE}(\mu_0 H_\perp = 100\,mT)$ as a function of $\Delta T(x)$ is also shown in Fig. (C). Shown in Fig. (D) is the time evolution of V_{ANE} that is measured at a fixed I = 3 mA and $\mu_0 H_\perp = 25$ mT, after switching off skyrmion generation currents (from 3.5 mA to 6 mA in 0.5 mA steps, Fig. E). Upon removing the increased DC currents used for generating skyrmions, discretized steps are gradually resolved.

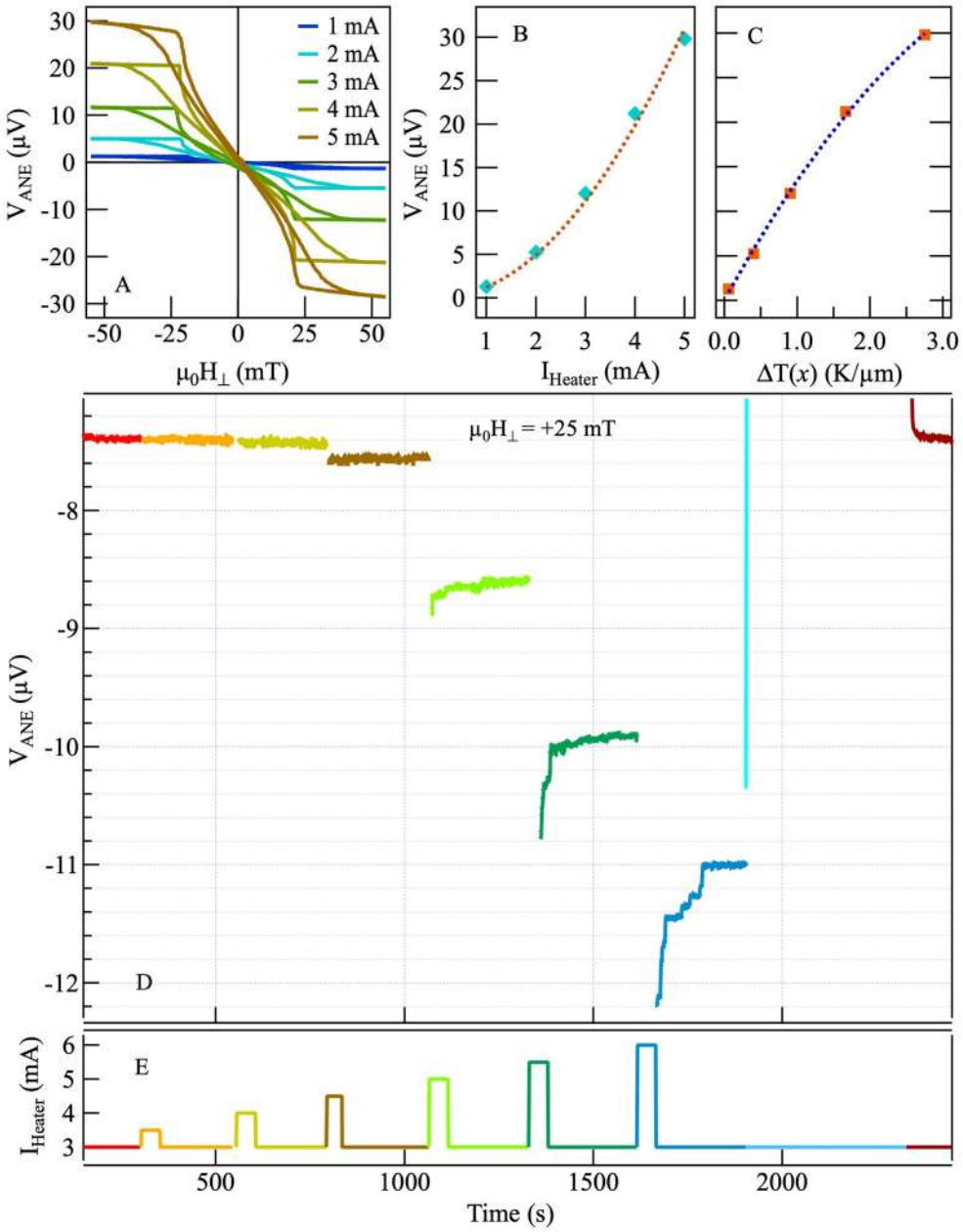
1 mA
2 mA
3 mA
4 mA
5 mA
A
V_{ANE} (μV)
$\mu_0 H_\perp$ (mT)
B
I_{Heater} (mA)
C
$\Delta T(x)$ (K/μm)
$\mu_0 H_\perp$ = +25 mT
D
E
I_{Heater} (mA)
Time (s)